Yield Function of the DOSimetry TELescope Count and Dose Rates Aboard the International Space Station

A. S. Caprotti[1,2], M. Brüdern[1], S. Burmeister[1] , B. Heber[1] , and K. Herbst[1]

[1]Institut für Experimentelle und Angewandte Physik, Christian-Albrechts Universität zu Kiel, Kiel, Germany, [2]Dipartimento di Fisica, Università degli Studi di Milano, Milan, Italy

Abstract The Earth is constantly hit by energetic particles originating from galactic sources. The flux of these particles is altered by the magnetized solar wind in the heliosphere and the Earth's magnetic field. For this reason, the ability of a particle to approach a spacecraft in low Earth orbit depends on its energy and the position of the spacecraft within the Earth's magnetosphere. Moreover, there are some areas (radiation belts) where the particles are trapped for a long time and, therefore, the flux of energetic particles is particularly high. Occasionally, solar energetic particles contribute to the energetic particle flux too. DOSimetry TELescope (DOSTEL) is one of the instruments aboard the International Space Station (ISS) that monitors the radiation field within the European module Columbus. Because being installed inside the ISS, particles produced by the interaction between the "primary" radiation and the ISS materials are also measured. To describe the observations in such a complex radiation field, we follow the method by Caballero-Lopez and Moraal (2012, *Journal of Geophysical Research*, 117[A12], A12103. doi:10.1029/2012JA017794) to compute the so-called yield function using precise measurements of the proton and helium energy spectra obtained by alpha magnet spectrometer and the systematic variation of the DOSTEL measurements within the Earth's magnetosphere.

1. Introduction

The radiation environment close to the Earth is dominated by energetic charged particles covering the energy range from below a few keV to about 10^{21} eV. At altitudes of about 400 km and with an orbital inclination of 51.6°, both the Earth magnetic field and the hull of the ISS shield astronauts against low energy cosmic rays. The origin of the particles that contribute most to the radiation dose is of galactic and solar or comes from the captured particles within the radiation belts (Xapsos et al., 2013). These trapped particles (primarily protons) are measured during passages of the so-called South Atlantic Anomaly (SAA). Of special interest is the radiation field within the ISS. Due to the interaction of energetic particles with the ISS material, this field differs significantly from the one outside and from the position of the station and within the station (see, e.g., Berger et al., 2017; Labrenz et al., 2015). However, the shielding is much lower than the one at sea level and might be compared to the radiation environment in the lower Earth stratosphere (Caballero-Lopez & Moraal, 2012). In addition to the shielding, the particle flux is altered by the Earth's magnetic field that can be approximated by a tilted dipole, which has an offset with respect to the Earth's center. As detailed below, different mathematical models exist to describe its geometry. As a consequence of this, one measures energetic particle fluxes at ISS altitudes that depend on the geomagnetic position (Labrenz et al., 2015, and references therein). During ground level enhancements, solar energetic particles (SEPs) are measured by instruments aboard the ISS (Berger et al., 2018, and references therein). In space physics research, the yield function of a detector (i.e., neutron monitor, muon telescope, etc.) is defined as the relationship between the intensity of primary cosmic rays and the counting rate of an instrument inside the atmosphere. As detailed below, the count rate depends on the geomagnetic position characterized by the so-called cutoff rigidity (see Equation 2). There are two ways to determine the atmospheric yield function. The empirical method is to measure the counting rate of an instrument inside simultaneously, and the primary spectrum outside the atmosphere (Aiemsa-ad et al., 2015; Mangeard et al., 2016, and references therein). The other method is to calculate the yield function using one of several generic numerical codes such as, for example, FLUKA (Böhlen et al., 2014) and GEANT4 (Agostinelli et al., 2003) to simulate the atmospheric cascade process, and then adding detector-specific details to these models (Mangeard et al., 2016; Mishev et al., 2020, respectively).
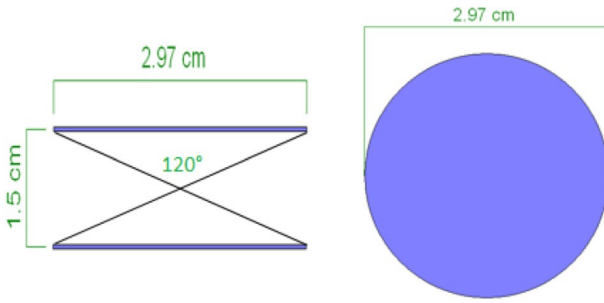
Figure 1. Sketches from the side (left) and top (right) of a DOSTEL.

When particles interact with human bodies and materials in the spacecraft, they deposit energy in the material. The energy per unit mass of the target is a quantity called dose (units: Gy). DOSIS 3D is an experiment aiming to study the dose distribution within the European Columbus module of the ISS. The active component of this experiment is the DOSTEL that measures the count and dose rates as a function of time. For more detail on the instrument and the measurements onboard the ISS, see (Labrenz et al., 2015). To describe the response function in such a complex radiation field, we follow the approach detailed in Caballero-Lopez and Moraal (2012) and determine the *yield function* empirically using precise measurements of the proton and helium energy spectra outside the Earth and the systematic variation of the DOSTEL measurements inside the ISS as a function of the cutoff rigidity. In what follows, we describe the instrument, the measurements utilized in our study, and the theoretical background. The yield function is then determined during two quiet periods that are times when the solar and Earth magnetic field activities are low.

2. Instrumentation

In 2012, the DOSIS3D experiment developed by Christian-Albrechts-University (CAU), Kiel (Germany) and Deutsches Zentrum für Luft und Raumfahrt (DLR), Köln (Germany) was installed inside the European Columbus Laboratory on board of the ISS. One of the main goals is to measure radiation exposure inside the ISS to estimate radiation risks for future missions. The instrument setup is composed of passive and active detectors: The first ones measure integrated values of the dose received during their exposure; the others provide real-time information. Each active detector is a DOSTEL. A previous version has been applied onboard several Space Shuttle missions of the European Space Agency (ESA) in the year 1996–1997 (Beaujean et al., 2002; Singleterry et al., 2001) and mounted on the MIR. In 2001, the instrument was mounted in the US Laboratory on the ISS as part of Dosimetry Mapping (DosMap), the first European Dosimetry experiment (Reitz et al., 2009). Between 2004 and 2011, a further version was used in the MATROSHKA experiment (Labrenz et al., 2015).

Each DOSTEL consists of two Passivated Implanted Planar Silicon (PIPS) detectors, each with a thickness of 315 μm and an area of 6.93 cm^2 arranged in a telescope geometry (see Figure 1). The distance between the two detectors is 1.5 cm. Both the opening angle and the geometric factor of the instrument are 120° and 824 mm^2 sr for particles in coincidence mode (i.e., hitting both the detectors: these are called "telescope" or linear energy transfer [LET] measurements). The instrument measures count rates and dose rates of radiation hitting a single detector ("dose measurement"). Each detector is sensitive to ions and electrons including minimum ionizing particles, photons in the energy range above the energy threshold of the detector as well as neutrons (Möller, 2008). Focusing on the dose measurements, the particle rate and the absorbed dose rate are stored in the DOSTEL memory after a certain time interval. To have a good statistic, this time interval is set to 100 s outside the region of the SAA, where the count rates are less than 30 per second. In the SAA, the time interval is chosen to be 20 s to improve time resolution. From these measurements, the absorbed dose rates are calculated. In contrast, the integration time for data in coincidence mode is about 45 min, and corresponding data sets are stored separately inside and outside the SAA as histograms of deposited energy. From the energy deposition spectra, LET spectra are derived to obtain the mean quality factor according to the Q(L) dependence given in ICRP60 (ICRP, 1991) as:

$$Q(L) = \begin{cases} 1 & \text{for } L < 10 \text{ keV} / \mu\text{m} \\ 0.32L - 2.2 & \text{for } 10 \le L \le 100 \text{ keV} / \mu\text{m} \\ \dfrac{300}{\sqrt{L}} & \text{for } L > 100 \text{ keV} / \mu\text{m} \end{cases} \tag{1}$$
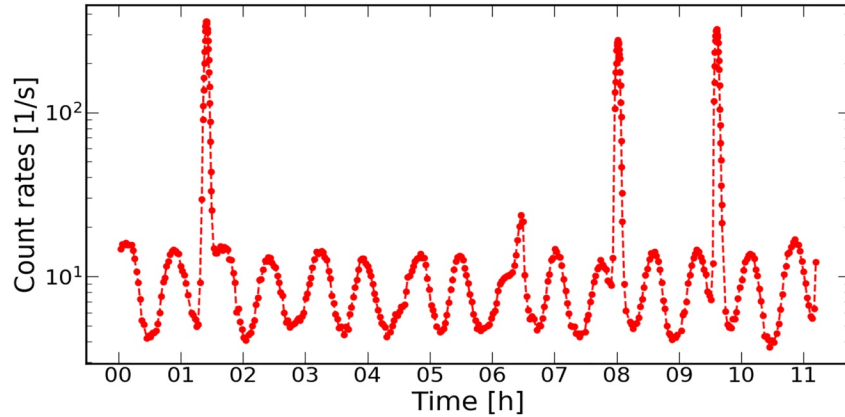
Figure 2. Count rates measured by DOSTEL for a sample of 11 h on January 1, 2014. The sudden count rate increases around 1:25, 6:28, 8:01, and 9:36 h correspond to crossings of the SAA, respectively.

Dose equivalent can be calculated by multiplying the mean quality factor to the measured dose. Due to the limited angle of incidence, the mean path length of 364 m in silicon is used to obtain the dE/dx in silicon. To convert dE/dx in silicon into dE/dx in water, the different stopping power of high energetic charged particles was used to calculate a mean conversion factor of 1.23. This approximation for the LET was concluded to be sufficient for dosimetry purposes. Since two DOSTEL instruments are mounted perpendicular to each other, information about the directionality of the radiation field inside the Columbus module can be determined (Berger et al., 2017).

3. Observations

Exemplarily, Figure 2 displays the observed count rate profile of the first half of January 1, 2014. Thereby, high and low count rates correspond to high and low latitudes, respectively. The sudden count rate increases around 1:25, 6:28, 8:01, and 9:36 h correspond to crossings of the SAA, respectively. In the following analysis, these data points are excluded.

The variation of the count rates depends significantly on the geomagnetic cutoff rigidity R_C. Thus, the count rate N is a function of R_C and is given by:

$$N(R_C, t) = \sum_i \int_{R_C}^{\infty} dR \, j_i(R, t) \, Y_i(R),$$ (2)

where $j_i(R, t)$ is the flux of incoming particles of the species i (proton, helium, $Z > 3$) and rigidity R at time t, and $Y_i(R)$ is the species-dependent yield function of the DOSTEL instrument. The yield function depends on the rigidity, because particles with higher rigidities are more likely to produce a large number of secondary particles. For the determination of the yield function, we follow the approach that was suggested by Caballero-Lopez and Moraal (2012). To do so, we had to perform the following tasks:

1. The cutoff rigidity dependency of the count rate $N(R_C)$ is approximated by the Dorman function (Dorman et al., 1970)

$$N(R_C) = N_0 \left[1 - \exp\left(-\alpha R_C^{\kappa}\right) \right],$$ (3)

1. with α and κ as free parameters depending on the altitude of the ISS and the phase in the solar cycle, respectively
2. The weight function $F_i(R)$ of each species i to an averaged yield function $Y(R)$ is determined.
3. The precise knowledge of the primary rigidity spectra $j_i(R)$ of each species utilizing flux data from alpha magnet spectrometer (AMS) published by Aguilar et al. (2018).

In the following sections, each of these required steps is discussed.

4. Theoretical Background

As mentioned above, DOSTEL data have to be analyzed to find the yield function of the instrument. The calculation requires a good description of the measured count rates within the Earth's magnetosphere by Equation 3, which further relates the DOSTEL count rates to cutoff rigidities. Note that the latter is computed from the geographical positions of the ISS obtained by great circle interpolations using ISS orbital data. Thus, the first step is to compute R_C using a certain model of the Earth's magnetic field (see Section 4.1) utilizing the PLANETOCOSMICS code described in Desorgher et al. (2009) (see Section 4.2). To facilitate the computation, some approximations have to be introduced, and their influence has to be investigated.

4.1. The Earth's Magnetic Field

Within a distance of about 6 R_E from the Earth's surface, the internal geomagnetic field can be approximated as a dipole, tilted with respect to the Earth's spinning axis by an angle of about 11°. Moreover, the center of the dipole is nearly 400 km far away from the Earth's center (Walt, 1994). For distances further out (>6 R_E) the magnetic field shape is significantly affected by the pressure of the solar wind: the field lines are squeezed on the dayside toward the Sun, and they cover a region within ~10 R_E from the Earth's surface. On the nightside, the lines are stretched, and they extend up to ≥50 R_E.

Semi-empirical models can describe the internal and external fields. In this study, we used the International Reference Geomagnetic Field (IGRF) model (Thébault et al., 2015, in particular IGRF-12) as a representation of the internal magnetic field, and the Tsyganenko "89 (TSY89) model representing the external magnetic field. The planetary magnetic field disturbance level is quantified by the so-called global K_p index, derived via experimental procedures. Every three hours, at 13 ground-based magnetic observatories in subauroral regions, variations of the horizontal components of the magnetic field are measured. Then, the variation range of each component (the difference between the highest and the lowest values) is considered. The measure of the largest range is associated with a certain value (between 0 and 9) of a local K_p index. As summarized in Tsyganenko (2013), the TSY89 model has further been improved (Tsyganenko'96 [TSY96], Tsyganenko '01 [TSY01], and recently Tsyganenko '05 [TSY05]). Nevertheless, as discussed in Tsyganenko (2013) the model results based on the TSY89 and the most recent TSY05 model show reasonable agreement for $k_p < 3$ conditions. Therefore, in this study, the TSY89 model was chosen to perform the simulations for the sake of simplicity, only requiring the K_p values as an input parameter. We note that only low K_p conditions ($k_p \leq 4$) are considered.

4.2. Computation of Vertical Cutoff Rigidities

The motion of charged particles in magnetic fields is described by particle rigidity (Desorgher et al., 2009; Shea et al., 1965). Although depending on the angle between the velocity of the particle and the magnetic field (pitch angle), we characterize the accessibility by the so-called vertical cutoff rigidity, the rigidity a particle has being measured by an upward pointing detector. Note, it is more difficult for charged particles in general to reach low latitudes than higher latitudes. Figure 3 shows the global distribution of the vertical cutoff rigidities modeled at an ISS altitude of 415 km. Different colors correspond to different cutoff rigidity values. Depending on cutoff rigidities, the count rates for a detector at a fixed altitude change with the geographical coordinates. This is illustrated by Picozza et al. (2013) in their Figure 13 showing PAMELA measurements at different altitudes. Their measurements show a steep intensity decrease at the rigidities below R_c. To derive these cutoff rigidity maps, we utilized the PLANETOCOSMICS code described in Desorgher et al. (2009): particles are generated at different rigidities at a given position at the altitude of the ISS and an incidence radial toward the center of the Earth (vertical direction). Computing their propagation in the geomagnetic field, for each particle a particle with an opposite charge is chosen that is injected at the given position and its direction opposite to the incoming direction (McCracken & Freon, 1962). This is known as the "backward-trajectory tracing method" and is described in Section 4.1. Note, that in PLANETOCOSMICS, not the planetary index K_p is used but a modified version of it, the option parameter IOPT (see Table A1) following the definition by Tsyganenko (1989) (see also Kudela & Usoskin, 2004).
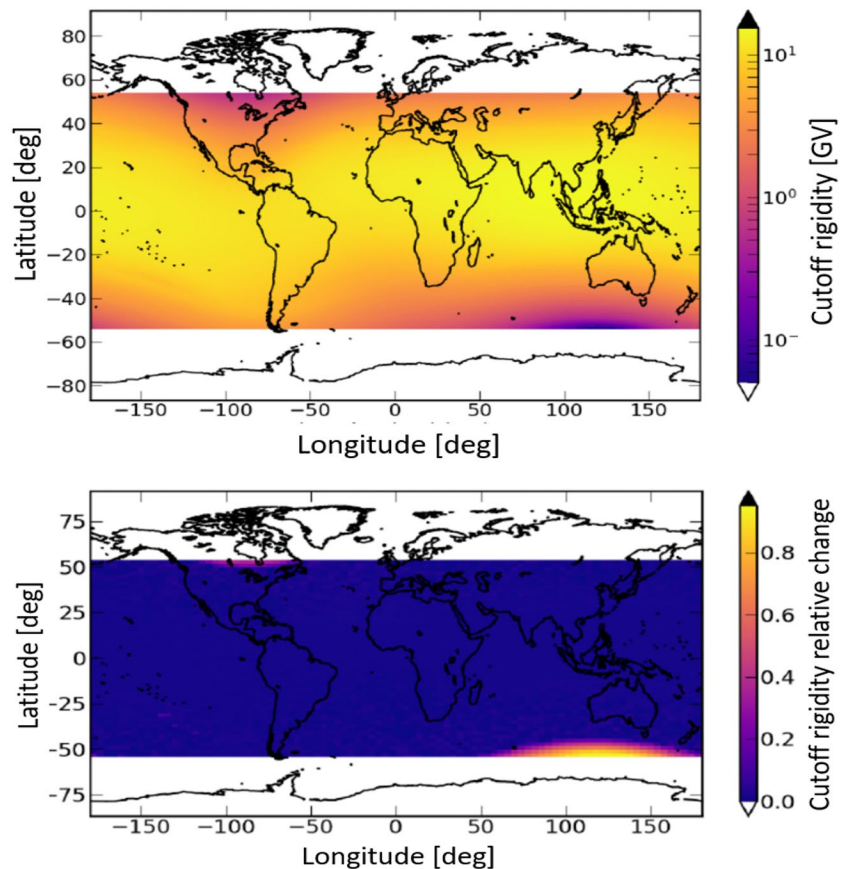
Figure 3. Upper panel: Vertical cutoff rigidities simulated with PLANETOCOSMICS for March 15, 2013 at an altitude of 415 km. The figure shows that the values decrease from the Equator to the poles. Lower panel: The relative difference in cutoff rigidity computed on March 13, 2013 at the minimum and maximum altitude of the ISS (399 and 440 km, respectively).

The altitude of the ISS changed between 399.322 and 439.865 km above the terrestrial surface during different maneuverd in 2013. To estimate the uncertainties due to the altitude variations, we calculated the cutoff rigidities for specific times and IOPTs, varying the altitudes among five chosen values. The starting time of the simulation was set to 15.00 UTC on 27 June 2014, with an IOPT value of 2 for the upcoming three hours. The lower panel of Figure 3 displays the relative differences in the computed cutoff rigidity values for an altitude of 399 and 440 km corresponding to the lowest and highest orbit altitude of the ISS, respectively. This is a good representation, since the ISS orbit varied only between 415 and 430 km in 2013. The corresponding relative differences range between 0 and nearly 1.

The differences increase with increasing latitude. A possible reason could be the following: near the Equator, even at different altitudes, the field lines crossed by the ISS are almost parallel to the Earth's surface and therefore to each other; going toward the poles, the field lines move closer to each other, and therefore they are not parallel anymore. The comparisons between the simulations revealed the highest relative error to be around 0.8 GV in a few bins at the highest latitudes considered. Comparing the lower panel of Figure 3 with the upper panel, we find that these regions correspond to cutoff rigidities up to some tenth of GV. In this study, only particles with a rigidity above ~0.5 GV are taken into account. For these particles, the altitude-dependent differences, however, are seldom that high. Moreover, the comparison is made for two situations with a very high altitude difference, which likely leads to an overestimation of the relative error.

Variation of the IOPT parameter in PLANETOCOSMICS: Our simulations require the K_p index as input, which is measured every 3 h. Therefore, we compute the cutoff rigidity assuming that K_p is constant within this time interval. The corresponding uncertainties are discussed in what follows. Figure 4 displays the
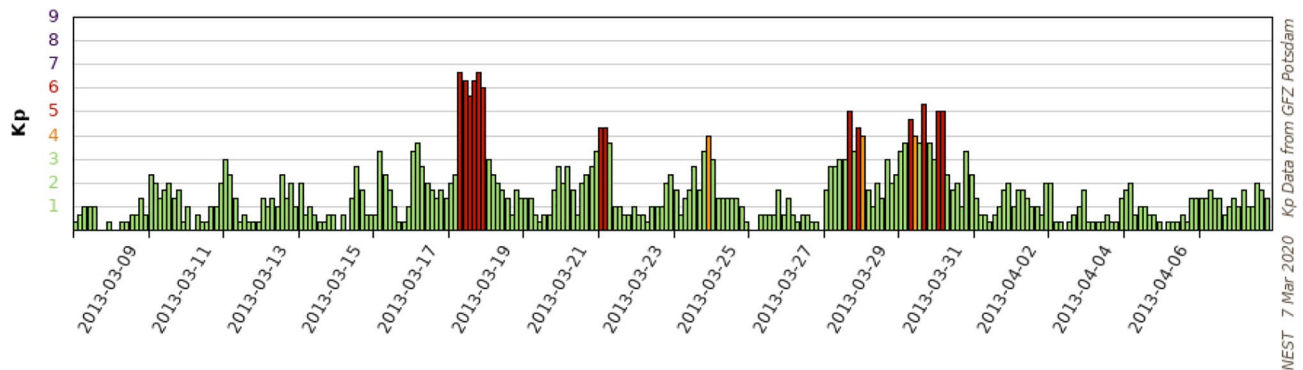
Figure 4. Variation of the 3-h planetary index K_p. There are time periods for which the K_p changes by a large amount (from nest.nmdb. eu).

variation of the 3-h K_p index from March 7, 2013 to April 7, 2013. The figure shows that the K_p index is highly variable and often changes by two from one to another interval. During extreme periods, the K_p even increases up to a value of 6 corresponding to an IOPT of 7. To estimate the differences between quiet (IOPT = 1) and active (IOPT = 7) phases, computations of the cutoff rigidity were performed for two specific periods. In addition, a period of an intermediate IOPT value of 4 has been investigated. Therefore, the conditions on 15 March 2013 (15:00 h, IOPT = 1), 17 March 2013 (12:00 h, IOPT = 7), and 15 March 2013 (03:00 h, IOPT = 4) at a mean ISS flight altitude of 415 km have been modeled. The upper panel of Figure 5 shows the relative differences between the model results utilizing IOPT = 7 and IOPT = 1, while the lower panel displays the moderate differences between IOPT = 1 and IOPT = 4, respectively. The differences are growing toward the poles, reaching values around 0.9 and 0.7, respectively, for a few bins at the very highest latitudes considered. In particular, when the IOPT is higher (upper panel of Figure 5) a high relative difference is also found at a certain distance from the highest latitudes. The comparison between the lowest and the extreme case (upper panel) as well as the comparison between the lowest and the moderate case can be utilized to estimate the uncertainty of the cutoff rigidity computations at a certain location. For most high-latitude locations, it is lower than 20% and 10% for the extreme and the moderate case, respectively. Although the TSY89 model is not a good approximation of the external magnetic field under extreme conditions (IOPT above 3) we used the computation to estimate the maximum uncertainties.

4.3. Time Corrections

As shown by Labrenz et al. (2013), the count as well as the dose rate measured by the DOSTEL need to be corrected for timing issues. In this study, the authors state: "The relation between count rate and R_c can be plotted for every 6-h data file, which covers four 90 min orbits of the ISS. To do this, orbit data of the ISS were used to get the corresponding location for each 100-s count rate interval." The R_c values, computed on a 1 ° × 1 ° grid, were used to get the R_c values of the corresponding positions. With this approach, we plot the measured count rates against the vertical geomagnetic cutoff rigidity values and determine the best time shift to obtain a distribution of measurements shown in Figure 6. Here, the blue line gives the fit of Equation 3. The corresponding parameters are summarized in the figure caption and Table B1 (Appendix B).

4.4. Computation of the Yield Function

The method used to calculate the yield function is the one reported in Caballero-Lopez and Moraal (2012). In a first step, Equation 2 can be re-written as

$$\frac{\partial N(R,t,x)}{\partial R} = \sum_i dR \, j_i(R) \, Y_i(R), \qquad (4)$$

where the term on the left reflects the differential count rate, which can be approximated by the derivative of the Dorman function given in Equation 3 (see also Dorman et al., 1970):
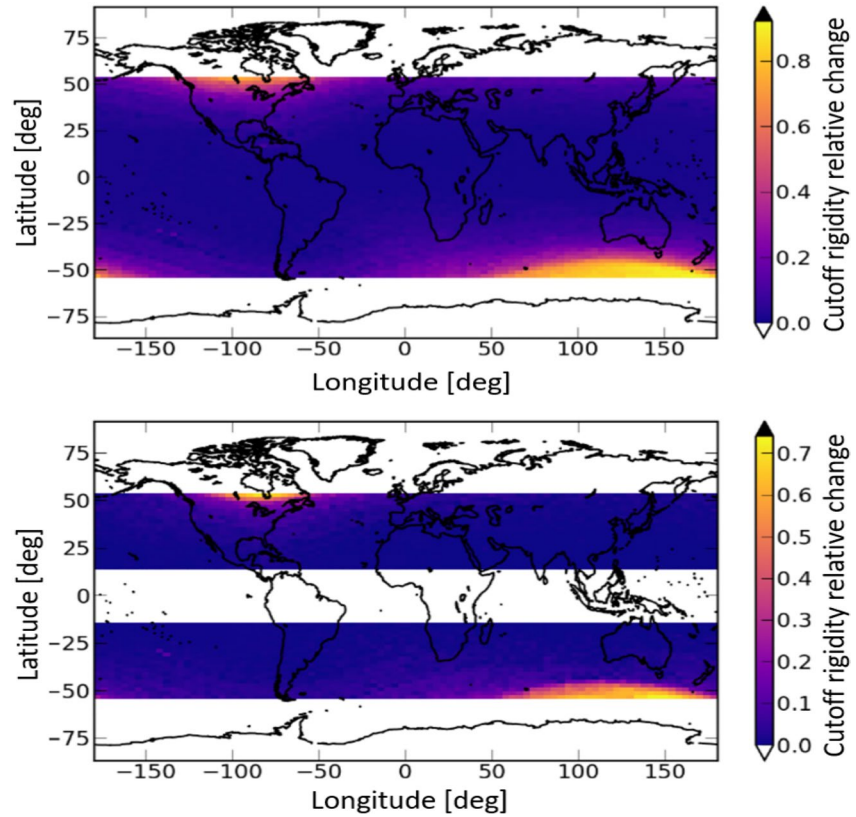
Figure 5. The two panels display the relative difference of the vertical cutoff rigidity maps on March 15, 2013 at 15:00 h and March 17, 2013 at 12:00 h are shown for IOPT = 1 and 7 as well as IOPT = 1 and 4 (on March 15, 2013 at 3:00 h), respectively. We note that only regions of large relative differences are shown in the lower panel.

$$\frac{dN(R_C,t)}{dR_C} = N_0 \cdot \alpha \cdot (k-1) \cdot R^k \exp(-\alpha \cdot R^{-k+1}). \tag{5}$$

According to Caballero-Lopez and Moraal (2012), the term on the right side of Equation 4 further can be simplified by

$$\frac{dN(R,t)}{dR} = j_H(R,t) \cdot Y_H(R) + j_{He} \cdot Y_{He} + j_{CNO} \cdot Y_{CNO} + j_{Other} \cdot Y_{Other}. \tag{6}$$

The proton yield function Y_H can be obtained as follows:

$$Y_H(R) = \frac{\dfrac{dN(R,t)}{dR}}{j_H(R,t) + j_{He}(R,t) \cdot \dfrac{Y_{He}(R)}{Y_H(R)} + j_{CNO}(R,t)}$$
$$\cdot \frac{Y_{CNO}(R)}{Y_H(R)} + j_{Other}(R,t) \cdot \frac{Y_{Other}(R)}{Y_H(R)} \tag{7}$$

Figure 6. DOSTEL count rates (red dots) as a function of vertical cutoff rigidity for the time period from May 20, 2015 to June 7 2015. The blue line is the result of the fit of Equation 3 to the data. The parameters found are $N_0 = 18.443 \pm 0.020$ 1/s, $\alpha = 4.044 \pm 0.0017$ GV, and $k = 1.013 \pm 0.001$ (see also Table B1). We note that the DOSTEL count rates have been obtained by filtering out data which were not within the two σ uncertainty band (green lines), where σ is calculated considering the counts disposed of in a Poisson distribution.

With the following approximations:

- the relative abundance ratios at 10.6 GV were taken from Gaisser et al. (2016) with 84.9%, 13.3%, 1.1%, and 0.8% for hydrogen, helium, CNO, and others, respectively;
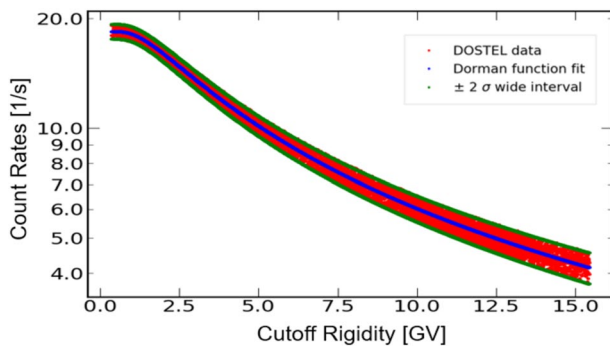
- for heavy ions ($Z \geq 4$) a $\frac{A}{Z}$ ratio of 2 has been assumed and, therefore, $Y_i(R) = \frac{Z}{2} Y_{He}(R)$;
- Clem and Dorman ([2000](#)) found a relation $\frac{Y_{He}(R)}{Y_H(R)} = F(R)$ from Monte Carlo simulations that has been approximated by Caballero-Lopez and Moraal ([2012](#)) in form of a double power-law depending on five parameters (Equation [10](#) given in Table [1](#)). the denominator can be written as

$$j_H(R) + F(R) \cdot J_{He}(R,t) \cdot \left(1 + 3.5 \cdot \frac{J_{CNO}(R.t)}{J_{He}(R,t)} + 5.6 \cdot \frac{J_{Other}(R.t)}{J_{He}(R,t)} \right), \tag{8}$$

and it can be reduced to

$$j_H(R) + 1.584 \cdot F(R) \cdot j_{He}(R,t) \tag{9}$$

when the relative abundance ratios are implemented. Thus, the proton yield function $Y_H(P)$ can be calculated from the measured hydrogen and helium rigidity spectra and the cutoff rigidity dependence of the instrument if the shielding/shooting differences between hydrogen and helium $F(R)$ is known. In the case of neutron monitors, this $F(R)$ was derived by Clem and Dorman ([2000](#)). The method developed by (Caballero-Lopez & Moraal, [2012](#)) follows an analysis through NM data, for which highly shielding conditions are valid. Taking into account that the shielding of the ISS is not exactly known and, thus, wrongfully may be assumed to be nearly negligible, the real conditions could correspond to values of F(R) well within the case of neutron monitors (solid red line in Figure [7](#)) with a shielding of 1,000 g/cm^2 and the case of no shielding (solid green line in Figure [7](#)). It shows that both cases differ significantly for rigidities below 3 GV. For more detail, Figure [8](#) shows the ratios between the highest and the lowest yield functions of the sample of the four quiet periods given in Table [2](#). As can be seen, the shielding effect becomes negligible for particles with energies above 3 GV.

However, although these substantial differences occur an approximation by a double power-law can be found

$$F(R) = F_0 (R_0^a + R^a)^{\frac{(\gamma_1 - \gamma_2)}{a}} \cdot R_2^{\gamma}, \tag{10}$$

with γ_1, γ_2, R_0, F_0 and a as the two spectral indices, the roll over rigidity, and the ratio at $R = \infty$, respectively. The corresponding parameters are summarized in Table [1](#).

5. Data Analysis

To determine the ISS DOSTEL specific yield function, we utilized the following equation:

$$Y_H(R) = \frac{\frac{dN(R,t)}{dR}}{j_H(R) + 1.584 \cdot F(R) \cdot j_{He}(R,t)} \tag{11}$$

resulting from Equations [7](#) and [9](#). To determine the quantities on the right side of this equation, we choose the following approach:

$\frac{dN}{dR}$: We selected four time periods that include a large number of days for which the planetary index K_p and, therefore, the IOPT is below 3. The start and end times of the selected periods and other corresponding quantities are summarized in Table [2](#). Note, that the ISS was for all periods in the +XVV configuration with one exception during the first period. A maneuver oriented the station to + ZVV on March 10, 2014 23:10 till March 11, 2014 00:11 then the station returned to + XVV. Since the time during the different orientation was short compared to the full period, we neglect the effect in what follows. However, the derived yield functions will therefore only be valid during the +XVV configuration.

1. During the second of the four periods (on May 20, 2015), an SEP event was registered by the Electron Proton Helium INstrument (EPHIN) aboard SOlar and Heliospheric Observatory (SOHO). As a com-
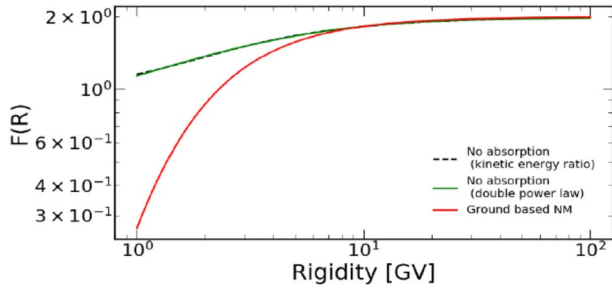
Figure 7. F(R) for no absorption condition (space-borne) represented by the kinetic energy ratio (dashed line) and a double power-law (green line). In comparison, F(R) of ground-based neutron monitors is shown by red line. The parameters for the two functions are listed in Table 1.

parison, the period-dependent 30 min averaged count rate variations of above 50 MeV protons are shown in the panels of Figure 9. Note that time profiles indicate variations of several percents during each period at rigidities below 2 GV (Kühl et al., 2015).

2. The approximation of the rigidity-dependent count rate profiles of the four periods utilizing the Dorman function given in Equation 3 is displayed in the panels of Figure B1. Table B1 summarizes the fit parameter and their uncertainties, while Figure B2 shows the differential spectra according to Equation 5.

j_H, j_{He}: The primary proton and helium fluxes measured with AMS are shown in the left and right panel of Figure 10, respectively. This experiment onboard the ISS measures the rigidity spectra for different ions in the range of a few GV up to several 100 TV. The relative precision of the fluxes is below ∼5%. The lower limit of the instrument is 1 GV for protons and 2 GV for helium (Aguilar et al., 2018). The data were obtained from https://tools.ssdc.asi.it/CosmicRays/and are given as 27 days averages up to 2017. Here, we utilized the files corresponding to the selected periods in Table 2. A double power-law was used to fit both proton and helium spectra. The parameters and their uncertainties are summarized in Table C1.

$F(R)$: The method developed by Caballero-Lopez and Moraal (2012) follows an analysis through NM data, for which high shielding conditions are valid. Bulk shielding of the ISS is substantial (Dobynde et al., 2019; Stoffle et al., 2012) but is approximately an order of magnitude less than that of neutron monitors. The effect of shielding on the yield function is important for rigidities less than 3 GV but of little importance at higher rigidity. Figure 7 shows F(R) for free space (green curve) and for typical neutron monitor shielding of 1,000 g cm⁻² (red curve). The cases are identical above 7 GV and differ only slightly between 3 and 7 GV. ISS shielding falls in between the two curves, closer to the free space case. For more detail, Figure 8 shows the ratios between the highest and the lowest yield functions of the sample of the four quiet periods given in Table B1. As can be seen, the shielding effect becomes negligible for particles with energies above 3 GV. The yield functions for both scenarios have been computed, and their differences are taken into account when computing the uncertainties.

Figure 11 displays the results for solar minimum conditions at the declining phase of solar cycle 24 in 2015. All yield functions agree very well for rigidities above 1 GV, however, showing significant deviations at cutoff rigidities below 0.6 GV. It is important to note that the error bands for the case of low modulation are calculated as the differences between the yield functions for each of the two periods, while in the case of high solar activity, the error band is calculated by propagating the uncertainties on the parameters resulting from the previous fits of the count rates and flux data. The increase of the latter uncertainty with decreasing

Figure 8. Ratio between the highest and the lowest yield functions of the sample of the four quiet periods is given in Table 2. The ratios are calculated based on Equation 11 (solid lines). In addition, the coefficient of F(R) is set to 0, therefore excluding the He contribution (dashed line). Here, a direct comparison between free space conditions (black curves) and neutron monitor conditions (red curve) is shown.

rigidity is due to the fact that the effect of the shielding is estimated by the extreme cases as detailed above. At rigidities below 2 GV the error is therefore largely overestimated. The second period in 2015 has been used to validate our approach by calculating the count rate rigidity profile from the yield function from the low modulation periods and the measured proton and helium spectra by AMS. From Equation 11, we get

$$N(R,t) = \int_{R_c}^{\infty} \frac{dN(R,t)}{dR} dR = \int_{R_c}^{\infty} Y_H(R) \cdot \left(j_H(R) + 1.584 \cdot F(R) \cdot j_{He}(R,t) \right) dR \tag{12}$$

with $Y_H(R)$ determined at solar minimum. The result is shown in Figure 12.

5.1. Yield Function for the Dose Rate

The method used to calculate the count rate yield function was applied to the dose rate measurements of DOSTEL. Therefore, the measured dose
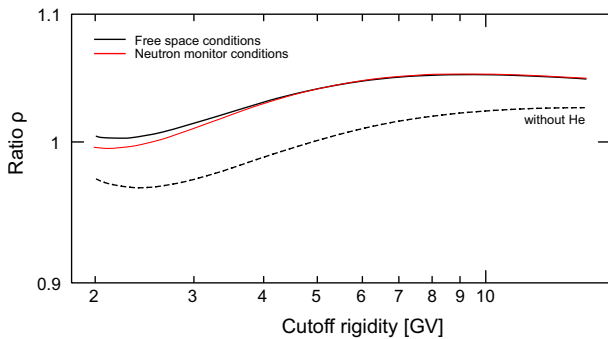
Table 1
Comparison of the Parameters of the Function F for Neutron Monitor and in Free Space

Parameters	Neutron monitor	Free space
F_0	2	2
P_0	0.45	5.5
A	1.4	1.4
γ_1	0	0
γ_2	10	0.4

rates were fitted with the Dorman function for the four periods. The result is summarized in Table B1. With χ^2-values between 1 and 1.5 for all four sets, the theoretical values are in good agreement with the measurements. An example is shown in Figure 13, where the calculated Dorman function is plotted together with the corresponding dose rate data sample. Following the discussion on the count rate yield function, we applied the same procedure including the uncertainties for the function $F(R)$ to the dose rates. However, due to the significant uncertainties below 2 GV, we decided to provide the averaged yield for the dose rate for vertical cutoff rigidities above 2 GV only as shown in Figure 14.

6. Summary and Conclusion

In this study, we determined the yield function for the count and dose rate of the DOSTEL that is part of the DOSIS 3D experiment onboard the ISS. Our analysis is based on the method suggested by Caballero-Lopez and Moraal (2012). To compute this function, the initial count and dose rate data have to be corrected for a time offset to relate them to cutoff rigidity values. To achieve this, we follow Labrenz et al. (2015) and calculated time- and space-dependent cutoff rigidities utilizing PLANETOCOSMICS (Desorgher et al., 2009). To reduce the computing time, simulations were performed once for three-hour intervals. During each period, we used the mean altitude of the ISS and magnetic field disturbance level IOPT. The Earth's magnetic field is modeled by the IGRF and the TSY89 model. This model has been shown to describe the Earth's magnetic field during low disturbance levels quite well. The analysis was, therefore, restricted to periods low planetary index K_p (<3). Four time periods of $\simeq$15–20 days between the years 2014 and 2017 were selected. An inspection of the proton flux at about 1 GV during these periods was performed. The first and second periods (March 2014 and May 2015) were influenced by remains of SEP events, which affected the result for these periods. Following the approach by Labrenz et al. (2015) the DOSTEL files were corrected for different time offsets. For this step, we computed from the ISS location in time the corresponding cutoff rigidities.

Following the steps described in Caballero-Lopez and Moraal (2012), the yield function of DOSTEL was computed. For this purpose,

1. the count and dose rate rigidity profiles were fitted by the Dorman function Equation 3;
2. the proton and helium fluxes were obtained from AMS- 02 for the time periods in question. The rigidity spectra were fitted by a double power-law; and
3. the function $F(R)$ is required, where R indicates rigidity. This function represents the computed ratio between the yield function for protons and helium. In our analysis, $F(R)$ for free-space conditions that means no absorption by the ISS to the incoming particles was approximated by a double power-law.

The yield functions were calculated for the periods in the declining and solar minimum phase of the solar cycle for rigidities above 2 GV only because the AMS helium spectra are only available above 2 GV. Due to extrapolation to lower rigidities and due to the complexity of the model, the determination of the function at lower rigidities is not reliable, and the fit parameters get highly correlated. In addition, the uncertainties

Table 2
Four Quiet Time Periods Associated with Long-term Low IOPT Values (IOPT < 4)

			Hours	Percentage	Modulation
Period	Start time	End time	Quiet times	Quiet times	Parameter in MV
1	March 2, 2014 3:00 UTC	March 21, 2014 12:00 UTC	435	92	652
2	May 20, 2015 6:00 UTC	June 7, 2015 15:00 UTC	435	97	660.5
3	September 8, 2016 12:00 UTC	September 24, 2016 21:00 UTC	357	90	436
4	April 26, 2017 3:00 UTC	May 15, 2017 6:00 UTC	414	95	363

The total hours and the relative contributions are quantified in the fourth and fifth column. The last column gives the modulation parameter ϕ from Usoskin et al. (2005).
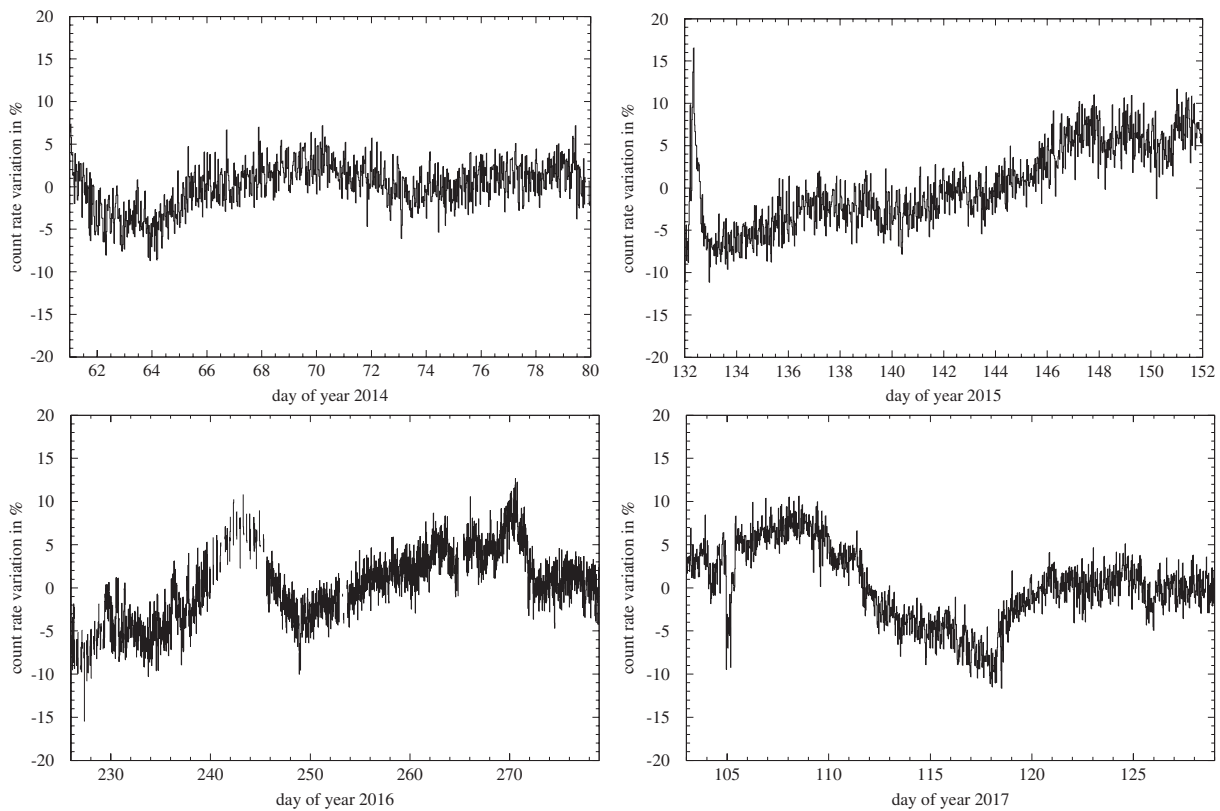
Figure 9. Count rates of the above 50 MeV/nucleon proton and helium channel (black curve) of the EPHIN on board SOHO for the four periods given in Table 2.

of all three steps above were taken into account, leading to large errors of the yield functions below 2 GV. The count rates of the first and second periods were computed to validate the method, using the AMS spectra. The comparison of the model with the measured count rates leads to a reasonable agreement, indicating that the description by the yield function can be used to compute the count rate variation for different levels of solar activity. To improve our approach, further periods need to be investigated and primary rigidity spectra should become available below 2 GV for helium and below 1 GV for protons.
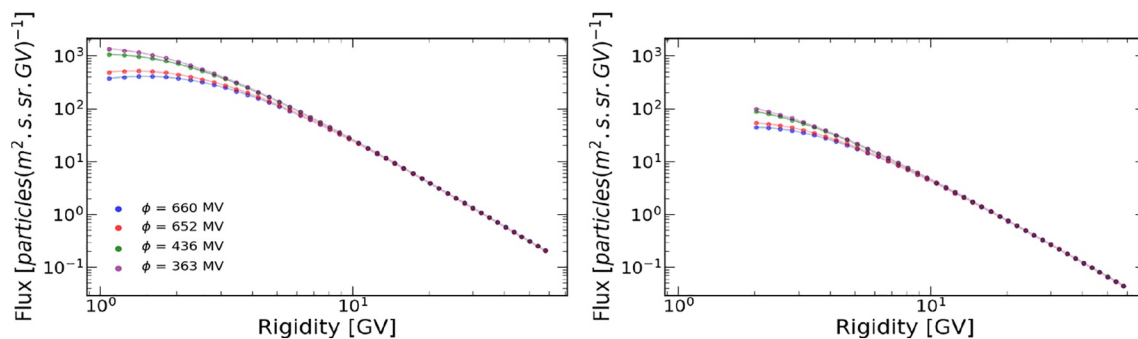

Figure 10. Energy spectra of protons (left panel) and helium (right panel) from AMS during the periods in Table 2. Different color-coding corresponds to periods of different solar activity. The corresponding modulation parameters ϕ have been taken from http://cosmicrays.oulu.fi/phi/Phi_mon.txt.
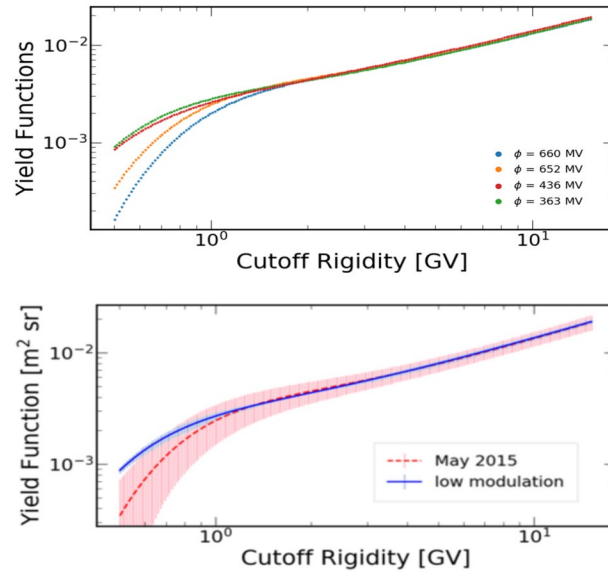
Figure 11. Upper panel: Yield functions for the four different modulation phases are shown in Figure 10 between 660 MV (in blue) and 363 MV (in green). Lower panel: The blue and red curve display the results of our analysis for the two periods at solar minimum in 2016 and 2017 (in blue) and during intermediate activity in 2015 (in red), respectively. We find a large deviation below 1 GV rigidity (for details, see text).
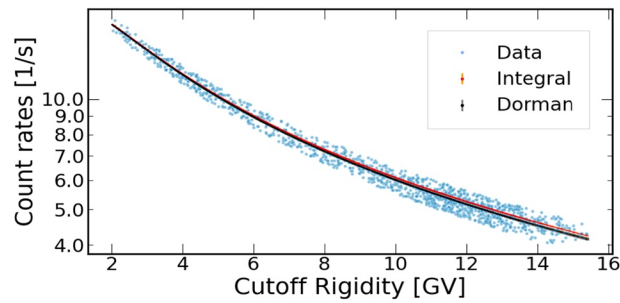

Figure 12. Measured count rates of the first period (blue dots). In addition, the approximation by the Dorman function (green line) and the Integral function derived by the yield function (Equation 12, red line) is shown.
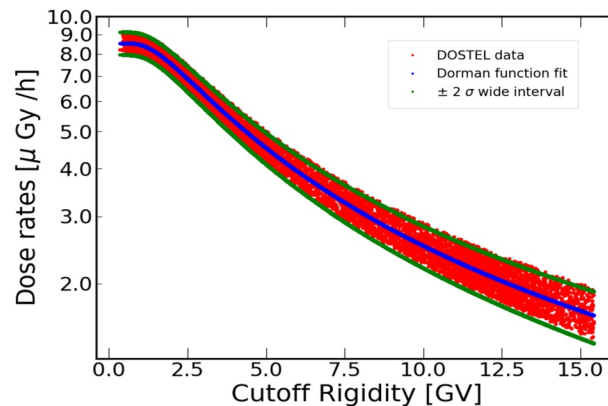

Figure 13. Dose rate measurement (red dots) and fit of the Dorman function to the data set for the second period. The resulting parameters are $N_0 = 8.513 \pm 0.015$ 1/s, $\alpha = 4.480 \pm 0.031$ GV, and, $k = 1.115 \pm 0.002$.
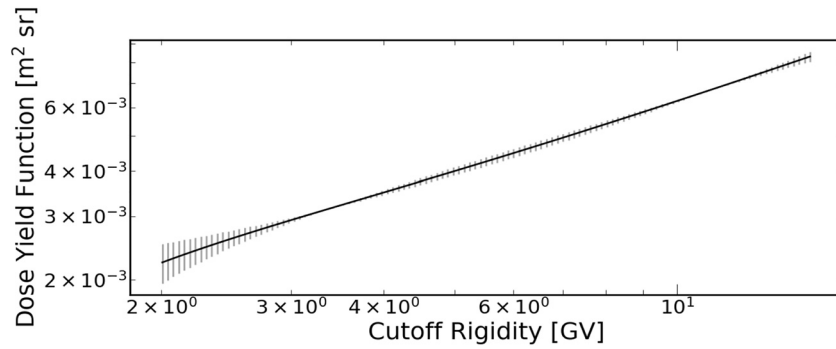
Figure 14. Average yield function calculated from the dose rates, valid for rigidities above 2 GV and shown by the black line.

Appendix: A and IOPT Relation

Table A1
Correspondence Between IOPT and K_p

K_p	0,0+	1−,1−1+	2−,2,2+	3−,3−3+	4−,4,4+	5−,5−5+	>6−
IOPT	1	2	3	4	5	6	7

Appendix B: Parameter of the Dorman Function

Table B1
Parameters for the Dorman Function During Periods 1 (March 2 to 21, 2014), 2 (May 20 to Jun 6, 2915), 3 (September 8 to 24, 2016), and 4 (April 26 to May14, 2017), respectively.

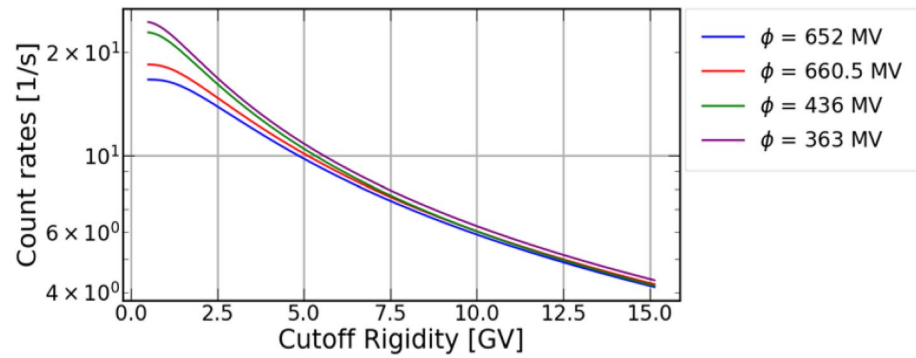|	Count rate fit parameters	χ^2		Dose rate fit parameters	
1	$N_0 = 16.674 \pm 0.017$ 1/s	1.044	1	$N_0 = 7.677 \pm 0.013$ 1/s	1.150
	$\alpha = 4.592 \pm 0.019$ GV^k			$\alpha = 5.081 \pm 0.036$ GV^k	
	$k = 1.022 \pm 0.001$			$k = 1.129 \pm 0.003$	
2	$N_0 = 18.443 \pm 0.020$ 1/s	1.051	2	$N_0 = 8.513 \pm 0.015$ 1/s	1.158
	$\alpha = 4.044 \pm 0.017$ GV^k			$\alpha = 4.480 \pm 0.031$ GV^k	
	$k = 1.013 \pm 0.001$			$k = 1.115 \pm 0.002$	
3	$N_0 = 22.944 \pm 0.030$ 1/s	1.068	3	$N_0 = 10.765 \pm 0.023$ 1/s	1.181
	$\alpha = 3.062 \pm 0.012$ GV^k			$\alpha = 3.455 \pm 0.023$ GV^k	
	$k = 1.002 \pm 0.001$			$k = 1.120 \pm 0.002$	
4	$N_0 = 24.618 \pm 0.033$ 1/s	1.085	4	$N_0 = 11.711 \pm 0.025$ 1/s	1.217
	$\alpha = 2.861 \pm 0.001$ GV^k			$\alpha = 3.039 \pm 0.019$ GV^k	
	$k = 0.991 \pm 0.001$			$k = 1.090 \pm 0.002$	

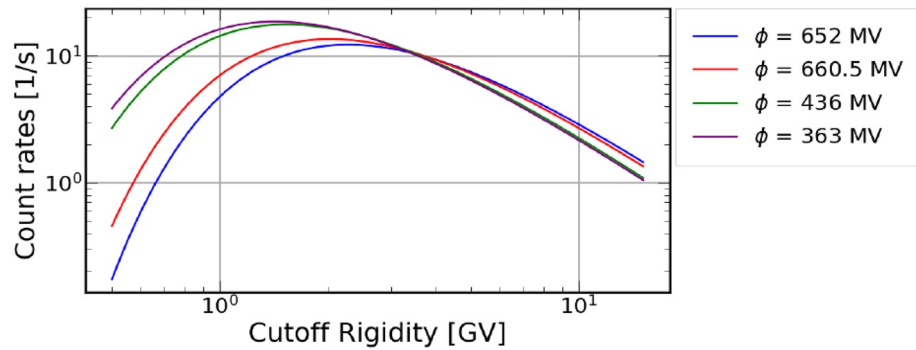**Figure B1.** Approximation of the averaged count rates measured during the four periods analyzed in this paper.

Figure B2. Differential count rate in the four periods analyzed (with rigidity $P > 2$ GV). Corresponding values of the modulation parameter ϕ are shown.

Appendix C: Fit Parameter for Rigidity Spectra

Table C1
Fit Parameters that Have Been Obtained for the Proton and Helium Spectra During the Four Periods to Approximate the AMS Rigidity Spectra with Equation 10

	Fit parameters (proton flux)	Fit parameters (helium flux)
1	$F_0 = 24{,}685.339 \pm 563.407$	$F_0 = 4084.205 \pm 97.040$
	$P_0 = 1.719 \pm 0.074$	$P_0 = 0.600 \pm 0.029$
	$a = 1.379 \pm 0.023$	$a = 1.192 \pm 0.011$
	$\gamma_1 = -2.872 \pm 0.005$	$\gamma_1 = -2.799 \pm 0.006$
	$\gamma_2 = 2.244 \pm 0.165$	$\gamma_2 = 11.653 \pm 0.705$
2	$F_0 = 23{,}158.911 \pm 638.625$	$F_0 = 3422.218 \pm 132.098$
	$P_0 = 1.569 \pm 0.100$	$P_0 = 0.800 \pm 0.119$
	$a = 1.407 \pm 0.032$	$a = 1.296 \pm 0.036$
	$\gamma_1 = -2.859 \pm 0.007$	$\gamma_1 = -2.760 \pm 0.009$
	$\gamma_2 = 2.288 \pm 0.256$	$\gamma_2 = 8.144 \pm 1.404$
3	$F_0 = 22{,}178.429 \pm 407.866$	3145.324 ± 91.825
	$P_0 = 1.101 \pm 0.087$	$P_0 = 0.800 \pm 0.011$
	$a = 1.360 \pm 0.028$	$a = 1.313 \pm 0.022$
	$\gamma_1 = -2.850 \pm 0.004$	$\gamma_1 = -2.738 \pm 0.007$

Table C1
continued

	Fit parameters (proton flux)	Fit parameters (helium flux)
4	$\gamma_2 = 2.626 \pm 0.351$	$\gamma_2 = 5.643 \pm 0.217$
	$F_0 = 23{,}344.391 \pm 789.663$	$F_0 = 3{,}502.970 \pm 132.089$
	$P_0 = 0.860 \pm 0.160$	$P_0 = 0.800 \pm 0.090$
	$a = 1.247 \pm 0.047$	$a = 1.122 \pm 0.027$
	$\gamma_1 = -2.858 \pm 0.008$	$\gamma_1 = -2.766 \pm 0.009$
	$\gamma_2 = 2.967 \pm 0.842$	$\gamma_2 = 4.214 \pm 0.775$

Data Availability Statement

AMS flux data are provided by the Space Science Database Center via the Cosmic Ray Database (https://tools.ssdc.asi.it/CosmicRays/). SOHO EPHIN and DOSTEL measurements can be obtained from http://ulysses.physik.uni-kiel.de/costep/and http://ulysses.physik.uni-kiel.de/exchange/publications/DOSTEL/, respectively.

References

Agostinelli, S., Allison, J., Amako, K., Apostolakis, J., Araujo, H., Arce, P., et al. (2003). Geant4—a simulation toolkit. *Nuclear Instruments and Methods in Physics Research Section A: Accelerators, Spectrometers, Detectors and Associated Equipment*, *506*(3), 250–303. http://www.sciencedirect.com/science/article/pii/S0168900203013688

Aguilar, M., Ali Cavasonza, L., Alpat, B., Ambrosi, G., Arruda, L., & Attig, N., & AMS Collaboration. (2018). Observation of fine time structures in the cosmic proton and helium fluxes with the alpha magnetic spectrometer on the International Space Station. *Physical Research Letter*, *121*(5), 051101. https://doi.org/10.1103/PhysRevLett.121.051101

Aiemsa-ad, N., Ruffolo, D., Sáiz, A., Mangeard, P.-S., Nutaro, T., Nuntiyakul, W., et al. (2015). Measurement and simulation of neutron monitor count rate dependence on surrounding structure. *Journal of Geophysical Research: Space Physics*, *120*(7), 5253–5265. https://doi.org/10.1002/2015JA021249

Beaujean, R., Kopp, J., Burmeister, S., Petersen, F., & Reitz, G. (2002). Dosimetry inside MIR station using a silicon detector telescope (DOSTEL). *Radiation Measurements*, *35*(5), 433–438. https://doi.org/10.1016/S1350-4487(02)00074-4

Berger, T., Burmeister, S., Matthiä, D., Przybyla, B., Reitz, G., Bilski, P., et al. (2017). DOSIS & DOSIS 3D: Radiation measurements with the DOSTEL instruments onboard the Columbus Laboratory of the ISS in the years 2009-2016. *Journal of Space Weather and Space Climate*, *7*, A8. https://doi.org/10.1051/swsc/2017005

Berger, T., Matthiä, D., Burmeister, S., Rios, R., Lee, K., Semones, E., et al. (2018). The solar particle event on 10 September 2017 as observed onboard the International Space Station (ISS). *Space Weather*, *16*(9), 1173–1189. https://doi.org/10.1029/2018SW001920

Böhlen, T. T., Cerutti, F., Chin, M. P. W., Fassò, A., Ferrari, A., Ortega, P. G., et al. (2014). The FLUKA code: Developments and challenges for high energy and medical applications. *Nuclear Data Sheets*, *120*, 211–214. https://doi.org/10.1016/j.nds.2014.07.049

Caballero-Lopez, R. A., & Moraal, H. (2012). Cosmic-ray yield and response functions in the atmosphere. *Journal of Geophysical Research*, *117*(A12), A12103. https://doi.org/10.1029/2012JA017794

Clem, J. M., & Dorman, L. I. (2000). Neutron monitor response functions. *Space Science Reviews*, *93*, 335–359. https://doi.org/10.1023/A:102650891526910.1007/978-94-017-1187-6_16

Desorgher, L., Kudela, K., Flückiger, E. O., Bütikofer, R., Storini, M., & Kalegaev, V. (2009). Comparison of Earth's magnetospheric magnetic field models in the context of cosmic ray physics. *Acta Geophysica*, *57*(1), 75–87. https://doi.org/10.2478/s11600-008-0065-3

Dobynde, M. I., Effenberger, F., Kartashov, D. A., Shprits, Y. Y., & Shurshakov, V. A. (2019). Ray-tracing simulation of the radiation dose distribution on the surface of the spherical phantom of the MATROSHKA-R experiment onboard the ISS. *Life Sciences and Space Research*, *21*, 65–72. https://doi.org/10.1016/j.lssr.2019.04.001

Dorman, L. I., Fedchenko, S. G., Granitsky, L. V., & Rishe, G. A. (1970). Coupling and barometer coefficients for measurements of cosmic ray variations at altitudes of 260-400 mb. *International Cosmic Ray Conference*.

Gaisser, T. K., Engel, R., & Resconi, E. (2016). *Cosmic rays and particle physics*. Cambridge, UK: Cambridge University Press.

ICRP. (1991). 1990 Recommendations of the International Commission on Radiological Protection (Vol. 60). ICRP Publication.

Kudela, K., & Usoskin, I. G. (2004). On magnetospheric transmissivity of cosmic rays. *Czechoslovak Journal of Physics*, *54*(2), 239–254. https://doi.org/10.1023/B:CJOP.0000014405.61950.e5

Kühl, P., Banjac, S., Heber, B., Labrenz, J., Müller-Mellin, R., & Terasa, C. (2015). Extended measurement capabilities of the electron Proton Helium INstrument aboard SOHO—Understanding single detector count rates. *Central European Astrophysical Bulletin*, *39*, 119–124.

Labrenz, J., Berger, T., Burmeister, S., Heber, B., & Reitz, G. (2013). On MATROSHKA/DOSTEL data interpretation. *International Cosmic Ray Conference 33*, 2302.

Labrenz, J., Burmeister, S., Berger, T., Heber, B., & Reitz, G. (2015). MATROSHKA DOSTEL measurements onboard the International Space Station (ISS). *Journal of Space Weather and Space Climate*, *5*, A38. https://doi.org/10.1051/swsc/2015039

Mangeard, P. S., Ruffolo, D., Sáiz, A., Madlee, S., & Nutaro, T. (2016). Monte carlo simulation of the neutron monitor yield function. *Journal of Geophysical Research: Space Physics*, *121*(8), 7435–7448. https://doi.org/10.1002/2016JA022638

Mangeard, P.-S., Ruffolo, D., Sáiz, A., Nuntiyakul, W., Bieber, J. W., Clem, J., et al. (2016). Dependence of the neutron monitor count rate and time delay distribution on the rigidity spectrum of primary cosmic rays. *Journal of Geophysical Research*, *121*(12), 620. 11,620–11,636. https://doi.org/10.1002/2016JA023515

McCracken, K. G., & Freon, A. (1962). Asymptotic directions and cut-off rigidities in the geomagnetic field. *Journal of the Physical Society of Japan Supplement*, *17*, 455.

Mishev, A. L., Koldobskiy, S. A., Kovaltsov, G. A., Gil, A., & Usoskin, I. G. (2020). Updated neutron-monitor yield function: Bridging between in situ and ground-based cosmic ray measurements. *Journal of Geophysical Research: Space Physics*, *125*(2), e2019JA027433. https://doi.org/10.1029/2019JA027433

Möller, T. (2008). *Charakterisierung eines dosimeters zur messung der ortsdosisleistung in flughöhen*. Christian-Albrechts-Universität zu Kiel.

Picozza, P., Marcelli, L., Adriani, O., Barbarino, G. C., Bazilevskaya, G. A., Bellotti, R., et al. (2013). Cosmic ray study with the PAMELA experiment. *Journal of Physics Conference Series*, *409*, 012003. https://doi.org/10.1088/1742-6596/409/1/012003

Reitz, G., Berger, T., Bilski, P., Facius, R., Hajek, M., Petrov, V., et al. (2009). Astronaut's organ doses inferred from measurements in a human phantom outside the International Space Station. *Radiation Research*, *171*(2), 225–235. https://doi.org/10.1667/RR1559.1

Shea, M. A., Smart, D. F., & McCracken, K. G. (1965). A study of vertical cutoff rigidities using sixth degree simulations of the geomagnetic field. *Journal of Geophysical Research*, *70*(17), 4117–4130. https://doi.org/10.1029/JZ070i017p04117

Singleterry, R. C., Badavi, F. F., Shinn, J. L., Cucinotta, F. A., Badhwar, G. D., Clowdsley, M. S., et al. (2001). Estimation of neutron and other radiation exposure components in low earth orbit. *Radiation Measurements*, *33*(3), 355–360. https://doi.org/10.1016/S1350-4487(01)00049-X

Stoffle, N., Welton, A., Barzilla, J., Gaza, R., Lee, K., & Zapp, N. (2012). CAD shielding analysis of the International Space Station. *17th Workshop on radiation monitoring for the International Space Station, 04–06 September 2012*, USA.

Thébault, E., Finlay, C. C., Beggan, C. D., Alken, P., Aubert, J., Barrois, O., et al. (2015). International geomagnetic reference field: The 12th generation. *Earth Planets and Space*, *67*, 79. https://doi.org/10.1186/s40623-015-0228-910.1186/s40623-015-0313-0

Tsyganenko, N. A. (1989). A magnetospheric magnetic field model with a warped tail current sheet. *Planetary and Space Science*, *37*(1), 5–20. https://doi.org/10.1016/0032-0633(89)90066-4

Tsyganenko, N. A. (2013). Data-based modeling of the Earth's dynamic magnetosphere: A review. *Annals of Geophys*, *31*(10), 1745–1772. https://doi.org/10.5194/angeo-31-1745-2013

Usoskin, I. G., Alanko-Huotari, K., Kovaltsov, G. A., & Mursula, K. (2005). Heliospheric modulation of cosmic rays: Monthly reconstruction for 1951–2004. *Journal of Geophysical Research*, *110*(A12), A12108. https://doi.org/10.1029/2005JA011250

Walt, M. (1994). Introduction to geomagnetically trapped radiation. *Cambridge Atmospheric and Space Science Series*, *10*.

Xapsos, M. A., O'Neill, P. M., & O'Brien, T. P. (2013). Near-earth space radiation models. *IEEE Transactions on Nuclear Science*, *60*(3), 1691–1705. https://doi.org/10.1109/tns.2012.2225846